Geolocating Time: Digitisation and Reverse Engineering of a Roman Sundial

Mara Pistellato[1 [0000−0001−6273−290X]], Arianna Traviglia[2 [0000−0002−4508−1540]], and Filippo Bergamasco[1 [0000−0001−6668−1556]]

[1] DAIS - Università Ca'Foscari, Via Torino 155, 30172, Venice, Italy
{mara.pistellato, filippo.bergamasco}@unive.it
[2] Istituto Italiano di Tecnologia (IIT), Center for Cultural Heritage Technology (CCHT), Via della Libertà 12, 30175 Venice, Italy
arianna.traviglia@iit.it

Abstract. The sundial of Euporus was discovered in 1878 within the ancient Roman city of Aquileia (Italy), in a quite unusual location at the centre of the city's horse race track. Studies have tried to demonstrate that the sundial had been made for a more southern location than the one it was found at, although no specific alternative positions have been suggested. This paper showcases both the workflow designed to fully digitise it in 3D and analyses on the use of the artefact undertaken from it. The final 3D reconstruction achieves accuracies of a few millimetres, thus offering the opportunity to analyse small details of its surface and to perform non-trivial measurements. We also propose a mathematical approach to compute the object's optimal working latitude as well as the gnomon position and orientation. The algorithm is designed as an optimization problem where the sundial's inscriptions and the Sun positions during daytime are considered to obtain the optimal configuration. The complete 3D model of the object is used to get all the geometrical information needed to validate the results of computations.

Keywords: Computational Archaeology, 3D Reconstruction, Reverse Engineering

1 Introduction

Digitisation and archiving play a fundamental role in cultural heritage field [13, 22]. Indeed, many technological applications are specifically designed to support such tasks, allowing for fast and precise results which were usually obtained through manual or analogue tools [20, 14]. In particular, 3D reconstruction offers a wide range of opportunities in terms of recording artefacts geometry, opening new research directions in terms of conservation, restoration and study [15, 11]. The reasons behind such applications are several: digital libraries of high-resolution 3D models bring to the creation of extensive archives, that can be available to a large audience of users, both in research and public communities. Digitisation also allows for restoration and monitoring of artworks which

Fig. 1. Left: Inscriptions on the top surface of the Euporus sundial. Right: 3D acquisition of the sundial: on the left the structured light scanner mounted on a tripod.

are often exposed to atmospheric agents. In particular, structured-light scanning techniques have already been employed in some cultural heritage applications, leading to optimal outcomes[2, 1, 21].

In this paper we describe a practical case study showing how structured-light scanning, and particularly phase-shift technique, can be applied in a cultural heritage application. We explore two main aspects regarding the study of an ancient sundial: its digitisation process and the reverse engineering approach determining the gnomon's shape and working latitude.

The object is hosted at the National Archaeological Museum of Aquileia (Italy), and it is known as the *"Sundial of Euporus"*, from the name of its donor, M. Anstitius Euporus, inscribed within the dial. The instrument was likely engraved in the 2nd century AD and was discovered in 1878 in the area of the Roman Circus of Aquileia, in centre of the horse race track [8], probably not in its original position. The object is a rare type of Karst limestone horizontal plane sundial (see Figure 1), pertaining to the Vitruvian type called *"plinthium sive lacunar"* [10], it is an horizontal slab surrounded by a frame, recalling the form of an overturned coffered ceiling [3]. The top planar surface measures 100×206 cm, and it is surrounded by a ~ 10 cm frame extending all around its rectangular shape (see Figure 1, right). A set of inscriptions located on one half of the upper surface reveals its usage as sundial (Figure 1, left).

The first part of the paper deals with the scanning process and focuses on the methodological aspects of the high-resolution acquisition. For the first time a complete 3D digitisation is attempted on this sundial, opening new possibilities in the analysis of its historical background and providing insights into the level of ancient knowledge of sundial design and construction principles. The complete 3D model enables to perform non-trivial studies without physically accessing the object, like analysing the technique used to chisel the inscriptions or the planarity of the dial surface, which affects the shadows cast by the gnomon.

In the second part of this work we present the reverse engineering technique adopted to recover the original gnomon's shape. This study exploits the 3D model to acquire precise measurements on the sundial's surface and create a

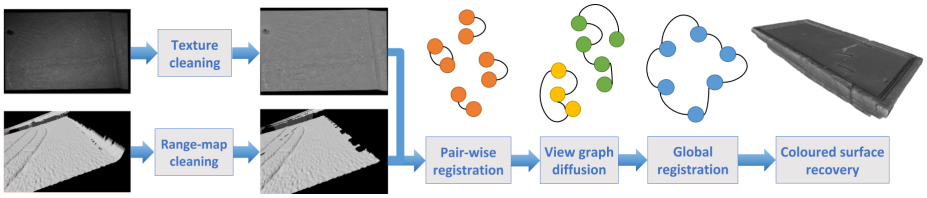

Fig. 2. Schematic representation of the 3D digitisation pipeline (see text for details).

synthetic model of its inscriptions. Then an optimization process is formalised and carried out to simultaneously compute the best gnomon configuration together with the optimal working latitude of the sundial.

2 3D Acquisition Process

The sundial digitisation was accomplished using a custom structured-light scanner formed by a camera and a projector (visible in Figure 1, right). The 3D reconstruction algorithm employs multi-period phase shift with the unwrapping and correction methods described in [16–18]. Additionally, the signal amplitude is used to get a high-resolution texture of the surface, since it captures the brightness intensity of the object as in a standard grayscale photograph.
Each scanner acquisition generates a *range-map*, that is a surface composed by the 3D triangulated vertices connected by triangles, and the corresponding texture map. Conceptually, the range-map is equivalent to a 3D photograph, capturing both the optical and geometrical properties of the surface.

The digitisation of the whole artefact cannot be performed with a single acquisition; indeed the area recorded by the scanner is not large enough to cover the entire object at a reasonable resolution, and its shape introduces occlusions in the opposite side of each view. For these reasons we acquired several overlapping portions of the surface to collect a set of "3D patches", corresponding to different range-maps. In this way, the entire artefact is recorded with high resolution, especially in the engraved zone. The following section describes the pipeline specifically designed to merge all the views and obtain the final reconstruction.

2.1 Reconstruction Pipeline

Starting from the acquired range-maps and textures, we designed a sequence of operations to reconstruct the complete coloured surface. Figure 2 presents a schematic representation of the tasks involved in the pipeline. They are the following: *pre-cleaning*, *pairwise matching*, *view graph diffusion*, *global registration* and *coloured surface recovery*. Such operations require almost no supervision: the user intervention is limited to the optional configuration of different task-specific parameters.

The most challenging part of the pipeline consists in merging all the individual range-maps: this procedure is referred as *registration* and it has been split

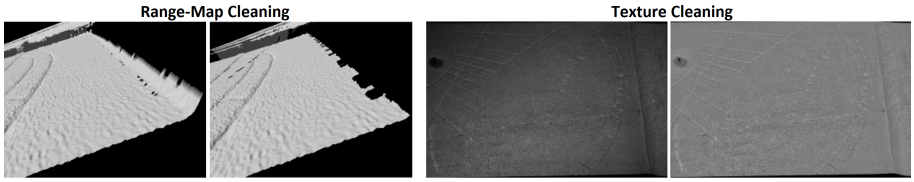

Fig. 3. Pre-cleaning results for range-maps (first and second images) and texture images (third and fourth).

in two steps. First, a pair-wise registration operates on each range-map pair to find the best possible rotation and translation that aligns the two. Second, all pairwise transformations are merged into a common 3D space through a global registration step. Finally, the complete surface is recovered by means of an automated algorithm which exploits the registered points and normals.

Texture and 3D Pre-cleaning The first two tasks entail a preliminary cleaning phase, in which range-maps and textures are independently processed to filter out noise and improve the photometric data quality.

Regarding the range-maps cleaning, the process involves (i) the removal of all triangles close to the surface border, (ii) the computation of per-vertex surface normal and (iii) the identification of small connected components that are removed below a certain threshold (we set 1000 vertices). The combination of such steps improves the quality of the range-maps, which are typically prone to exhibit errors near the boundaries of the illuminated area. A visual example of the effect of this cleaning process is shown in Figure 3.

For what concerns the textures, the goal of the cleaning process is to normalise the uneven illumination exhibited by the intensity images. Indeed, surface areas that are far away from the projector's centre will appear darker than the other ones: the effect is visible in Figure 3 (third image). To correct this phenomenon, we normalized each texture by means of an high-pass filter designed to remove the low-frequency light variations and thus preserving the high-frequency details of the texture, which are in our interests. This operation was performed with a non-linear top-hat operation using a disc-shaped structuring element of size 51×51. In Figure 3 (fourth image) we show an example of resulting image texture after the correction. After all the images have been processed, they can be put side by side with no evidence of texture borders or light changes, allowing for a natural range-maps fusion.

Pair-wise Registration Given the feature-rich nature of the object surface, the pair-wise registration step was implemented by matching feature points between every couple of views. We exploited well-known SIFT features [12] to provide a set of point-to-point correspondences between each couple of textures. Each

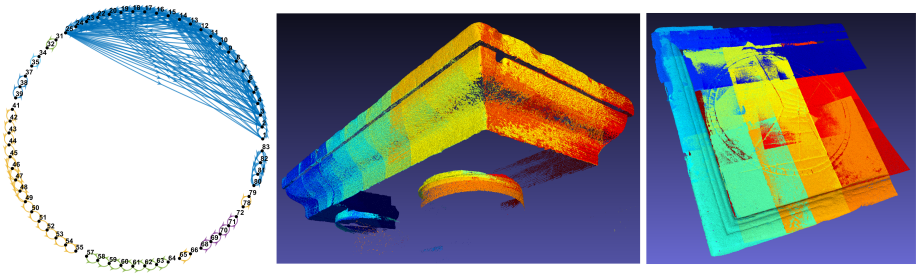

Fig. 4. Left: the view graph. Each node represents a range-map and each edge a pairwise transformation (see text for details), the connected components are denoted by different colours. Centre: the yellow component (graph nodes from 41 to 55) forms part of the outer frame. Right: the blue component (nodes from 1 to 25) connects all the range-maps acquired in the engraved area.

range-map associates a 3D point coordinate to each 2D point on the texture image, therefore the computed feature matching produces two sets of corresponding 3D points in space. Such correspondences are exploited to compute the relative transformation between two views, allowing the registration of the range-maps as described in [6].

Since some possible matching errors would significantly affect the alignment precision, a RANSAC-based algorithm [4] was adopted to select only the consistent 3D matches and obtain the best transformation between point clouds. The quality of the alignment is measured in terms of inliers, i.e. couples of 3D points for which distance after the transformation is below a threshold (1 mm). This ensures a minimum level of precision for each registration: all the pairwise transformations exhibiting at least 20 inliers were included in the so-called view graph, described in the next paragraph.

View-Graph Diffusion A view graph is used to group the computed transformations: each node represents an acquired range-map, while each edge denotes the transformation between such views. In other words, when an edge is present, it indicates a valid transformation between two overlapping acquisitions: therefore each connected component represents a group of range-maps that can be merged to obtain a portion of the whole object.
In Figure 4 (left) the complete view graph is displayed: each connected component is identified by a different colour. Due to small estimation errors, within a connected component different paths between two views would result in two inconsistent transformations. In order to compute a coherent set of transformations within each group of views, a state-of-the-art diffusion technique was applied as described in [24], ensuring the overall error minimisation for each set. After the diffusion, the range-maps belonging to a connected component are merged to form a macro-section of the sundial. In Figure 4 (centre and right) the merged range-maps coming from the two largest components are shown.

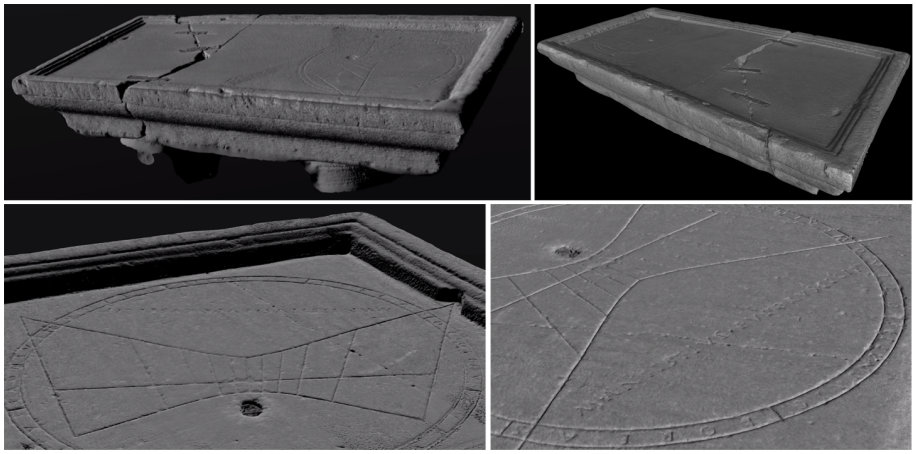

Fig. 5. Some views of the final coloured model after Poisson surface reconstruction. Top: the whole scanned artefact. Bottom: details of the sundial engraving.

Global Registration and Surface Reconstruction The global registration step involves the joining of the surfaces obtained from each connected component of the graph. First, a rough registration is performed in a semi-automatic way by manually selecting some correspondence points. Then, to refine the alignment all the components are registered using ICP (Iterative Closest Point) algorithm [25]. Finally, the surface of the sundial was computed applying Screened Poisson Reconstruction method [7]. This algorithm generates closed watertight surface which interpolates all the given points: the output is a set of coloured points and triangles reconstructing the entire object.

2.2 Reconstruction Results

Since the most relevant part of the sundial is the engraved zone, the acquisition process was planned to capture such area with a higher accuracy with respect to the rest. The acquisition was performed in two sessions: first, the scanner was configured to acquire an area of approximately 40x30cm, at a distance of ∼100 cm in order to obtain a high-resolution for the main inscriptions. We acquired 40 range-maps with this configuration: the first 25 were acquired closer to the object, while the rest covered more surface in order to help the global registration of each view. All acquired views were planned so that the overlapping portion of each range-map with its successive was at least $\frac{1}{3}$ of its area. The second session entailed a change of the scanner optics in order to acquire a wider area (approximately 150x200 cm) at a distance of 250 cm. We acquired 45 range-maps all around the whole artefact, capturing both the outer frame and the planar surface. For each range-map, an average of 6.5 million triangles composed from ∼5 million 3D points were acquired. After the global registration, each range-map was resampled to obtain a roughly uniform distribution of the 3D points among

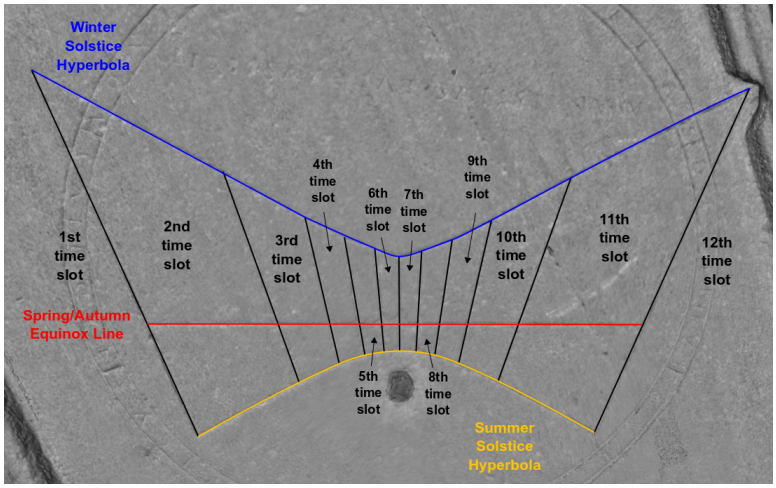

Fig. 6. Time slots displayed by the sundial, each one denotes an equal subdivision of daylight. Solstice hyperbole and equinox line are also highlighted.

all the connected components. The final surface was created using the screened Poisson reconstruction algorithm with a tree depth set to 11 and 3 samples per node. Figure 5 shows the model of the scanned artefact in its entirety (top row) and some details of the sundial engraving (bottom row). The overall resolution is high enough to allow the analysis not only of the whole artefact, but also of the micro-furrows, scratches and unevenness of surface.

3 Gnomon Reverse Engineering

From ancient times, sundials were manufactured with the purpose of measuring time from the apparent position of the sun in the sky. Usually sundials comprise an object casting a shadow (the gnomon) and a surface, where the shadow is casted, in which some marks indicate the time or the current part of the day. Ancient sundials usually divide daylight time (i.e. from sunrise to sunset) into equal parts. For this reason the construction of such objects is easier and longitude correction is not needed, since it does not point the "clock time" as we are used today. Indeed, since daylight has a variable duration depending on day and latitude, each "time slot" does not have the same duration throughout the year.

The line connecting the Sun with the tip of the gnomon describes a cone in a frame which is rotating with the Earth. The shadow of the tip is therefore located on the intersection between that cone and the sundial plane, forming a conic section depending on the displacement of the plane containing the Sun apparent path and the celestial equator (in which the tip lies). Most of the days the conic section is an hyperbola, more or less curved, becoming a line twice a year during the equinoxes, when light and night times have the same duration.

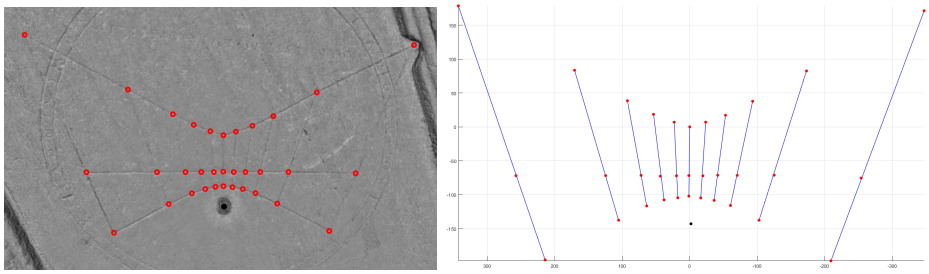

Fig. 7. On the left, the 3D points acquired from the model; on the right, the corresponding 2D points used for optimization. All measures are displayed in mm.

Figure 6 highlights the salient curves engraved in the studied sundial. Two hyperbole are visible (depicted in blue and yellow), indicating the path traced by the shadow of the gnomon's tip during winter and summer solstices. The horizontal red line is the equinox line, traced by the shadow during two days, in autumn and spring. Finally, the engraved part of the object includes eleven segments used to mark the time during the day (in black).

3.1 Dial Parametrisation

To reverse engineer the Euporus' sundial, we first need to localise all the marks on the sundial's plane. We recovered those points from the 3D reconstruction of the artefact, ensuring a measurement precision of about a millimeter and the computation non-trivial features, such as the object's planarity.

We computed the coordinates of 34 points in three-dimensional space from the intersections between equinox and solstices curves with the 11 time marks. Figure 7 (left) shows a detail of the 3D model and the extracted points: three for each time mark (in red) plus the gnomon's base (in black). Note that the time marks are not perfectly symmetric with respect to the central line (the sixth), that corresponds to the south-north axis. The acquired points were transformed to a convenient reference frame: a plane was fitted to the 34 intersection points to define a *geographical frame* with the y-axis (coinciding with the sundial's main axis) facing north, x-axis faces east and z-axis oriented upward. The applied transformation does not affect the final result since the sundial's axis must be aligned with the North-South axis to work properly.

The measured points are almost coplanar with a maximum distance from the fitted plane of ~ 0.8 mm. Therefore, we can assume the points to lay on the plane (so that their z coordinate is zero) without loss of precision in the following computations. The result of model acquisition is shown in the rightmost part of Figure 7. After normalization, the point coordinates on the sundial's plane (apart from the gnomon's base) are arranged in a rank 3 tensor $V_{\alpha\beta\gamma}$ with $\alpha \in \{1, 2, 3, 4\}$ denoting respectively spring equinox, summer solstice, autumn equinox and winter solstice, $\beta \in \{1, \dots, 11\}$ identifying the β^{th} intersection point with the time marks and $\gamma \in \{1, 2\}$ the 2D coordinate of the point. Note that

points with $\alpha = 1$ and $\alpha = 3$ are identical since the projection during the two equinoxes must correspond.

3.2 Formalization of Sundial Functioning

In order to introduce the notation that will be used in the following parts, we define the following sets:

- $Y \subset \mathbb{Z}$: set of years (BC negative, AC positive).
- Δ: set of dates s.t. $d \in \Delta$ indicates a day in the format (year, month, day).
- T: set of timestamps. Each element $t \in T$ encodes a date and a time. A timestamp can be interpreted as a sequence of values of the kind (year, month, day, hour, minutes, seconds).
- $L = [-90, 90]$: set of latitudes (in degrees).

Suppose to have a function which returns the Sun's position given a latitude and a timestamp:

$$S(t, l) : T \times L \to \mathbb{S}^2 \tag{1}$$

where $\mathbb{S}^2$ is the set of 3D vectors belonging to the surface of a unitary sphere. The result of such function is a unit vector which points at the Sun's position during timestamp t at latitude l.

As we already discussed, the sundial's marks do not indicate the "clock" time, but the current fraction of light-time, that has been equally split. Therefore, we are only interested in the light time of each day, and not in the real clock time as we were calibrating a clock. In other words, given a date and a place on Earth we just need to compute the 12 time slots, without considering the so-called apparent solar time. For this reason we have no need of longitude corrections, thus our formulation restricts to latitude only, fixing the longitude value in all the computations. Moreover, the geographic area involved in the research is quite narrow in terms of longitude, but it exhibits a wider latitude range. Considering that the optimal working location of the object is extremely sensitive to latitude changes (especially for what concerns the hyperbole curves and equinox line), the longitude can be considered irrelevant for our purposes.

The projection of a generic 3D point on the sundial's plane can be computed considering a projective system in which the Sun is the centre, located at infinity, emitting light rays to be projected on the sundial's plane as a parallel projection [5]. The resulting projection $\mathbf{p}'$ of a 3D point $\mathbf{p}$ on a plane is computed as follows:

$$\mathbf{p}' = \begin{pmatrix} \mathbf{r}_1^T \\ \mathbf{r}_2^T \end{pmatrix} \left(\mathbf{p} + \frac{-\mathbf{p} \cdot \mathbf{n}}{\mathbf{n} \cdot \mathbf{s}} \mathbf{s} \right) \tag{2}$$

where $\mathbf{s}$ is the vector pointing at Sun's position computed as in (1), and $\mathbf{n}$ is a unitary vector representing the normal direction of the plane (i.e. perpendicular to it) in which the shadow is casted. Finally, $\begin{pmatrix} \mathbf{r}_1 & \mathbf{r}_2 & \mathbf{n} \end{pmatrix}^T$ is the rotation matrix

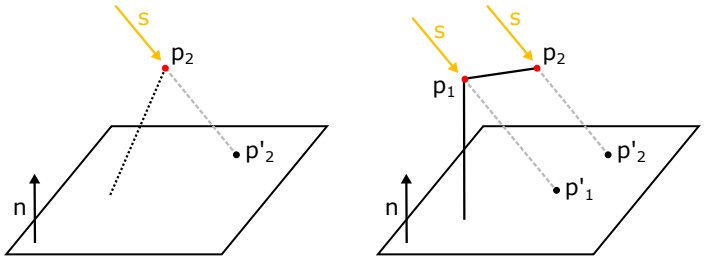

Fig. 8. Left: punctual projection, with unknown gnomon configuration. This setup is sufficient to estimate p_2 coordinates as well as the optimal latitude. Right: presumed gnomon configuration. Points p_1 and p_2 are projected on the plane, forming a segment.

transforming the sundial's plane to our geographical plane. Note that we used the first two rows of the matrix so that the final projected point is a 2D point.

We model the gnomon through two junction points, characterizing the shadow's length and slope. The end of the vertical part will be identified as $\mathbf{p}_1$, while the endpoint of the tilted part is $\mathbf{p}_2$. Figure 8 displays a schematic representation of the projection. In particular, points and vectors involved in Equation 2 are included (the apostrophe denotes the projection of the point).

3.3 Recovery of the Optimal Gnomon's Geometry

Since the sundial works with 12 equally-spaced time slots during daylight, we define a utility function H such that $H(d, l) : \Delta \times L \rightarrow T^{11}$. Given a date d and a latitude l, such function computes the 11 timestamps which should correspond to the marks on sundial's plane. Note that each timestamp marks the transition from one slot to the following one, as sketched in Figure 6: the first mark denotes the end of the first slot and the beginning of the second, and so on. Our goal is to estimate the parameters so that the gnomon's shadow is projected as close as possible to the corresponding marks at the timestamps returned by function H.

We divided the operation in two independent tasks: (i) the joint optimization of p_2 and the latitude and (ii) the computation of p_1 and thus the inclination of the gnomon. The choice is driven by the following observations: the sundial's working latitude is only affected by the projection of point p_2 during equinoxes and solstices. In fact, the endpoint of the shadow casted by the gnomon must fall exactly on those curves in four specific days in a year. In this terms, we can forget the gnomon's shape and consider only a punctual projection of p_2 onto the plane (see Figure 8, left). During the four relevant days such projection must overlap with the corresponding curve.

Once the point p_2 is fixed, and hence the latitude is recovered, the shadow's inclination allows to guess a possible shape for the whole gnomon. In particular, we assume a single joint in correspondence of point p_1. This task could be affected

by the thickness of the stick, and requires a different criterion to assess the correctness of the projection.

Latitude Optimization For the sundial to work we need the shadow of the gnomon's tip p_2 to occur in some predefined points during four days every year. Each of these days is associated with a curve and, in turn, each curve is marked with eleven points corresponding to the time slots dividing each day.

Solstices and equinoxes days slightly change each year, thus we define a utility function $\hat{D}(y)$ which returns four dates from Δ corresponding to equinoxes and solstices in year y. These dates are computed as follows: summer and winter solstices are the dates in which the daylight is respectively maximum and minimum (between 20-22 June and 20-23 December), while the two equinoxes are days in which daylight is equal to night time (19-21 March and 21-24 September).

The function $P(y, l, \mathbf{p}_2, \mathbf{n})$ computes a rank 3 tensor, with a structure analogue to V, containing the projections of 3D point $\mathbf{p}_2$ at each of the 11 timestamps of each four dates in $\hat{D}(y)$.

In an ideal configuration the coordinates of the computed projections in P perfectly overlap with the sundial's points in V. In practice the projection can not be perfect, so we aim to minimize the squared distance of all the projections from the corresponding sundial's points. Thus, we formulate the following non-linear least square problem:

$$(l^*, \mathbf{p}_2^*, \mathbf{n}^*) = \underset{l, \mathbf{p}_2, \mathbf{n}}{argmin} \quad \sum_{y \in Y} (\bar{P} - \bar{V})^T (\bar{P} - \bar{V}) \tag{3}$$

where $\bar{V}$ and $\bar{P}$ are the linearized 88-elements row vectors of the tensors $V_{\alpha\beta\gamma}$ and $P(y, l, \mathbf{p}_2, \mathbf{n})$ and the set Y contains a list of years in which solstices and equinoxes dates have been computed. With this formulation we optimize simultaneously the latitude, the gnomon's vertex and the normal of the sundial's plane in such a way that the sum of the distances from the casted shadows to the target points is minimized. Note that the minimization is non-linear due to the function (1) used in P.

Gnomon's Inclination Optimization In this second step, we keep fixed the coordinates of p_2, the latitude and the plane normal as the optimal values obtained in the previous task, so that the position of p_1 has an impact only on the shadow's shape and inclination. Indeed, in this setup the role of p_1 is simply aesthetic because the oblique part of the gnomon projects a segment which should be aligned with the eleven sundial's marks to ease the time reading.

For this reason the position of p_1 is estimated such that its punctual projection falls as close as possible to the line of the corresponding time mark, determined by the current time slot. Since the original gnomon was supposed to rise vertically from its base, the only parameter we need to optimize is the junction's height. The coordinates of point $\mathbf{p}_1$ are:

$$\mathbf{p}_1 = (x_0, y_0, h)^T \tag{4}$$

where (x_0, y_0) are the coordinates of the gnomon's base (Figure 7, the black point) and h is the elevation of the junction point.

Similarly to what we did for p_2, we define a function $\mathcal{P}(d, l, \mathbf{p}_1, \mathbf{n})$ returning a rank 2 tensor $\mathcal{P}_{\beta\zeta}$ describing the eleven projections (in homogeneous coordinates, with $\zeta \in \{1 \dots 3\}$) of point $\mathbf{p}_1$ during day d at latitude l. Such projections are computed in correspondence of the eleven timestamps that split the daylight of d into twelve equal time slots. Note that, unlike the previous function P (computed in four particular days of a year), $\mathcal{P}$ is defined for a single day, since we want the projection of p_1 to be close to the engraved segments during all days and not only during solstices and equinoxes.

We also need to express the parameters of the eleven lines containing the segments of the sundial. In a 2D Euclidean plane, a line can be denoted as $\ell = (a, b, c)$ such that a point (x, y) lies on the line if $\ell \cdot (x, y, 1) = 0$.

We collect these values in a rank 2 tensor $\mathcal{V}_{\beta\zeta}$ such that

$$\mathcal{V}_{ij} = \frac{\ell_i}{||\ell_i||} \tag{5}$$

and $\ell_i = (a_i, b_i, c_i)$ are the three parameters of the i-th line lying on the plane. Then, we minimize the squared distance of such projections from the correspondent line engraved on the sundial's surface. Considering $\bar{\mathcal{P}}$ the linearized row-vector of $\mathcal{P}(d, l, \mathbf{p}_1, \mathbf{n})$, the energy function to be minimized is now:

$$h^* = \underset{h}{argmin} \quad \sum_{y \in Y} \sum_{d \in D(y)} (\bar{\mathcal{P}} \cdot \bar{\mathcal{V}})^2. \tag{6}$$

The optimization task is performed selecting a set of years Y and the corresponding sets $D(y)$ containing all the valid dates in y. Unlike the previous energy function, $\mathcal{P}$ is linear since equation (1) can be pre-computed for the given dates. Therefore, a global minimum can be found through simple linear least squares.

4 Results

Both the optimization tasks were performed over a set of several years to provide a robust estimation of the gnomon's configuration and latitude. Therefore, we chose a set of years in which the sundial were in use and optimized the configuration for that specific period. To compute the correct Sun's position given a place, time and a date, we used the open-source library Pvlib [23], implementing the Solar Position Algorithm [19]. Such algorithm ensures a precision of ± 0.0003 degrees between the years 2000 BC and 6000 AD.

The joint optimization of the gnomon's tip p_2 and the latitude was performed computing the solstices and equinoxes from 200 AD to 230 AD and minimizing the energy function (3). The Nelder-Mead simplex algorithm for function optimization has been used, as described in [9]. Such method is a numerical algorithm used in multidimensional optimization problems for which derivatives are not known, like in our case where the Sun position function is not derivable.

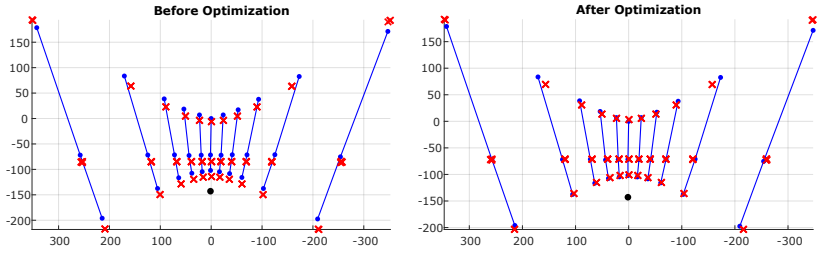

Fig. 9. Projections (red crosses) of point p_2 during equinoxes and solstices before (left) and after (right) optimization of latitude and point p_2. The rightmost configuration exhibits a better overlap between projections and sundial's points.

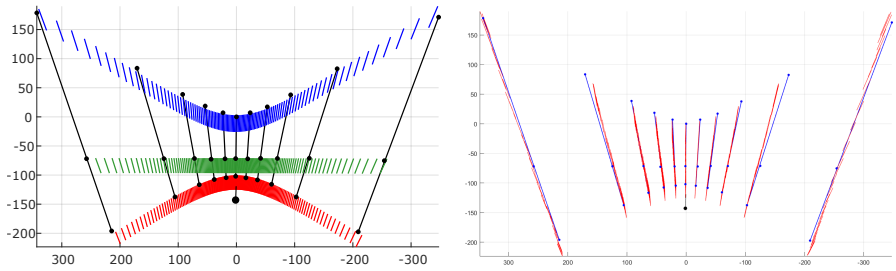

Fig. 10. Final configuration results. Left: shadows projected during daylight time in winter solstice (blue), autumn and spring equinoxes (green) and summer solstice (red). Right: shadows projected during a whole year (every 10 days), in correspondence of the eleven sundial's time marks.

The initial latitude was set at 45.46° North (Aquileia latitude) and the gnomon's endpoint was positioned in a plausible way such that its shadows fall close to the ideal points lying on the solstices and equinoxes curves. The plane normal was also initialised as $\mathbf{n} = (0, 0, 1)$, that is perfectly parallel with respect to the ground. The initial configuration is displayed in Figure 9 (left), in which each red cross marks the shadow projected by the gnomon's endpoint p_2 during the selected days of the period.

The optimization took around 250 iterations to converge, setting a maximum tolerance over both the energy values and the optimized value equal to 10^{-5}. Surprisingly, the estimated optimal working latitude of the sundial was 44.019 N (in decimal notation), which is roughly 160 km south of Aquileia. As for the plane normal vector $\mathbf{n}$, each test did not change its orientation, so we kept the sundial's plane parallel to the ground. The estimated gnomon's endpoint has final coordinates $p_2 = (23.8225, -0.0007, 50.1031)$. Figure 9 (right) displays the shadows cast by p_2 in the optimized configuration: We observe a good overlap between the majority of the sundial's marks and the projected shadows. Also, points corresponding to the earliest and latest hours of winter solstices are not perfectly aligned. This could be caused by errors in the sundial design, since the shadows in these specific times are longer and thus more difficult to estimate.

Regarding the junction point p_1, we optimized its height over all days of the selected years, resulting in an optimal value $h = 47.97$ mm. Figure 10 displays the results obtained with the complete optimal configuration of the gnomon. The leftmost plot shows the set of shadows projected during the day respectively in: winter solstice (in blue), summer solstice (red) and equinoxes (green). Note that the inclination of the projected segment is almost parallel to the engraved lines and the top part of the shadows points at the two hyperbole and the line. The rightmost plot shows the shadows (in red) projected during a whole year in correspondence of the timestamps that denotes the change of timeslots in which each day is divided. Note that the inclination of the shadows is almost always parallel to the sundial segments, as expected if p_1 is correctly estimated.

Finally, we virtually rendered the shadow casted after the gnomon estimation to verify if it coincides with the marks of the sundial at equinoxes and solstices. Figure 11 shows three rendered pictures with the computed gnomon and the projected shadow for interesting days of the year.

5 Conclusions

The scanning of the Euporus sundial is the first step of a more in-depth analysis to be undertaken on the artefact. The reconstruction provides a high quality 3D shape record of the sundial's surface with measurement accuracy to the millimetre level and serve as a fine 3D representation that can be used for documentation, research and conservation purposes.

Moreover, the 3D model supported a further analysis to determine the geographical location for which the sundial was designed and shaped. In particular, a mathematical analysis of the gnomon's projection and the relative optimization process shown that the optimal working latitude for this kind of configuration is indeed a southern location with respect to the place where the object was discovered (lat 44.019 N, while Aquileia latitude is 45.79 N). A plausible hypothesis is that the Euporus sundial inscription was copied from another object designed for more southern latitudes, and perhaps some calculation errors caused its slightly defective functioning in Aquileia area.

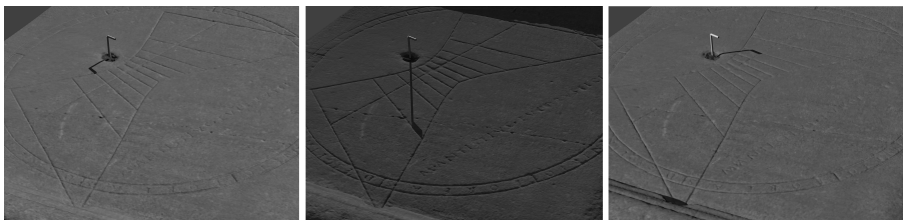

Fig. 11. Digital rendering of the sundial with a simulated gnomon as computed in our optimization process. The Sun position was set according to the optimal latitude. Pictures show the casted shadow during (from left to right): summer solstice, winter solstice and equinox.

References

1. Akca, D., Remondino, F., Novák, D., Hanusch, T., Schrotter, G., Gruen, A.: Recording and modeling of cultural heritage objects with coded structured light projection systems. In: 2nd International Conference on Remote Sensing in Archaeology. pp. 375–382. Institute of Geodesy and Photogrammetry, ETH Zurich (2006)
2. Akça, M.D.: 3d modeling of cultural heritage objects with a structured light system (2012)
3. Auber, P.A.: L'orologio solare orizzontale del circo di aquileia (ii sec. d.c.). il "plintio di euporus". prima parte. Atti dell'Istituto Veneto di Scienze, Lettere ed Arti, Classe di scienze fisiche, matematiche e naturali **CLXIII (2004-2005) 231-298**
4. Fischler, M.A., Bolles, R.C.: Random sample consensus: a paradigm for model fitting with applications to image analysis and automated cartography. Communications of the ACM **24**(6), 381–395 (1981)
5. Hartley, R., Zisserman, A.: Multiple view geometry in computer vision. Cambridge university press (2003)
6. Horn, B.K.: Closed-form solution of absolute orientation using unit quaternions. Josa a **4**(4), 629–642 (1987)
7. Kazhdan, M., Hoppe, H.: Screened poisson surface reconstruction. ACM Transactions on Graphics (ToG) **32**(3), 29 (2013)
8. Kenner, F.: Sonnenuhren aus aquileia, mittheilungen der k.k. central-commission zur erfortschung und erhaltung der kunst und historischen denkmale. VI Jahrgang, Neue Folge, Wien (1880)
9. Lagarias, J.C., Reeds, J.A., Wright, M.H., Wright, P.E.: Convergence properties of the nelder–mead simplex method in low dimensions. SIAM Journal on optimization **9**(1), 112–147 (1998)
10. Lancaster, L.C.: Concrete vaulted construction in Imperial Rome: innovations in context. Cambridge University Press (2005)
11. Li, R., Luo, T., Zha, H.: 3d digitization and its applications in cultural heritage. In: Euro-Mediterranean Conference. pp. 381–388. Springer (2010)
12. Lowe, D.G.: Distinctive image features from scale-invariant keypoints. International journal of computer vision **60**(2), 91–110 (2004)
13. Lynch, C.: Digital collections, digital libraries & the digitization of cultural heritage information. Microform & imaging review **31**(4), 131–145 (2002)
14. Müller, G., Bendels, G.H., Klein, R.: Rapid synchronous acquisition of geometry and appearance of cultural heritage artefacts. In: VAST. pp. 13–20 (2005)
15. Pieraccini, M., Guidi, G., Atzeni, C.: 3d digitizing of cultural heritage. Journal of Cultural Heritage **2**(1), 63–70 (2001)
16. Pistellato, M., Bergamasco, F., Albarelli, A., Cosmo, L., Gasparetto, A., Torsello, A.: Robust phase unwrapping by probabilistic consensus. Optics and Lasers in Engineering **121**, 428–440 (2019). https://doi.org/10.1016/j.optlaseng.2019.05.006
17. Pistellato, M., Bergamasco, F., Cosmo, L., Gasparetto, A., Ressi, D., Albarelli, A.: Neighborhood-based recovery of phase unwrapping faults. vol. 2018-August, pp. 2462–2467 (2018). https://doi.org/10.1109/ICPR.2018.8546052
18. Pistellato, M., Cosmo, L., Bergamasco, F., Gasparetto, A., Albarelli, A.: Adaptive albedo compensation for accurate phase-shift coding. vol. 2018-August, pp. 2450–2455 (2018). https://doi.org/10.1109/ICPR.2018.8545465
19. Reda, I., Andreas, A.: Solar position algorithm for solar radiation applications. Solar energy **76**(5), 577–589 (2004)

20. Santagati, C., Inzerillo, L., Di Paola, F.: Image-based modeling techniques for architectural heritage 3d digitalization: limits and potentialities. International Archives of the Photogrammetry, Remote Sensing and Spatial Information Sciences **5**(w2), 555–560 (2013)
21. Sitnik, R., Krzeslowski, J.F., Maczkowski, G.: Archiving shape and appearance of cultural heritage objects using structured light projection and multispectral imaging. Optical Engineering **51**(2), 021115 (2012)
22. Stanco, F., Battiato, S., Gallo, G.: Digital imaging for cultural heritage preservation: Analysis, restoration, and reconstruction of ancient artworks. CRC Press (2011)
23. Stein, J.S., Holmgren, W.F., Forbess, J., Hansen, C.W.: Pvlib: Open source photovoltaic performance modeling functions for matlab and python. In: 2016 ieee 43rd photovoltaic specialists conference (pvsc). pp. 3425–3430. IEEE (2016)
24. Torsello, A., Rodola, E., Albarelli, A.: Multiview registration via graph diffusion of dual quaternions. In: CVPR 2011. pp. 2441–2448. IEEE (2011)
25. Zhang, Z.: Iterative point matching for registration of free-form curves and surfaces. International journal of computer vision **13**(2), 119–152 (1994)